Supporting Online Materials

For

Microwave assisted synthesis, microstructure and physical properties of Rare-Earth Chromites

Jesús Prado-Gonjal[1], Rainer Schmidt[2*], Juan-Jose Romero[3], David Ávila[1], Ulises Amador[4], Emilio Morán[1]

[1] *Dpto. Química Inorgánica, Facultad de CC. Químicas, Universidad Complutense de Madrid, 28040 Madrid (Spain)*

[2] *Dpto. Física Aplicada III, Facultad de CC. Físicas, GFMC, Universidad Complutense de Madrid, 28040 Madrid (Spain)*

[3] *Instituto de Ceramica y Vidrio, CSIC, C/Kelsen 5, 28049 Madrid (Spain)*

[4] *Dpto. Química, Facultad de Farmacia, Universidad San Pablo - CEU, 28668 Boadilla del Monte - Madrid (Spain)*

*Corresponding author. Email: rainerxschmidt@googlemail.com

Part I. X-ray diffraction & Rietveld refinement parameters

Supporting Online Materials (SOM) Figure 1 shows the powder X-ray diffraction (XRD) patterns of the (RE)CrO_3 series. Tables 1a and 1b summarize all structural parameters obtained from Rietveld refinements of the XRD pattern using FullProf software and the χ^2, R_{wp}, R_{exp} and R_B values obtained for each fit. Tables 2a and 2b summarize additional parameters such as bonding angles and bonding distances.

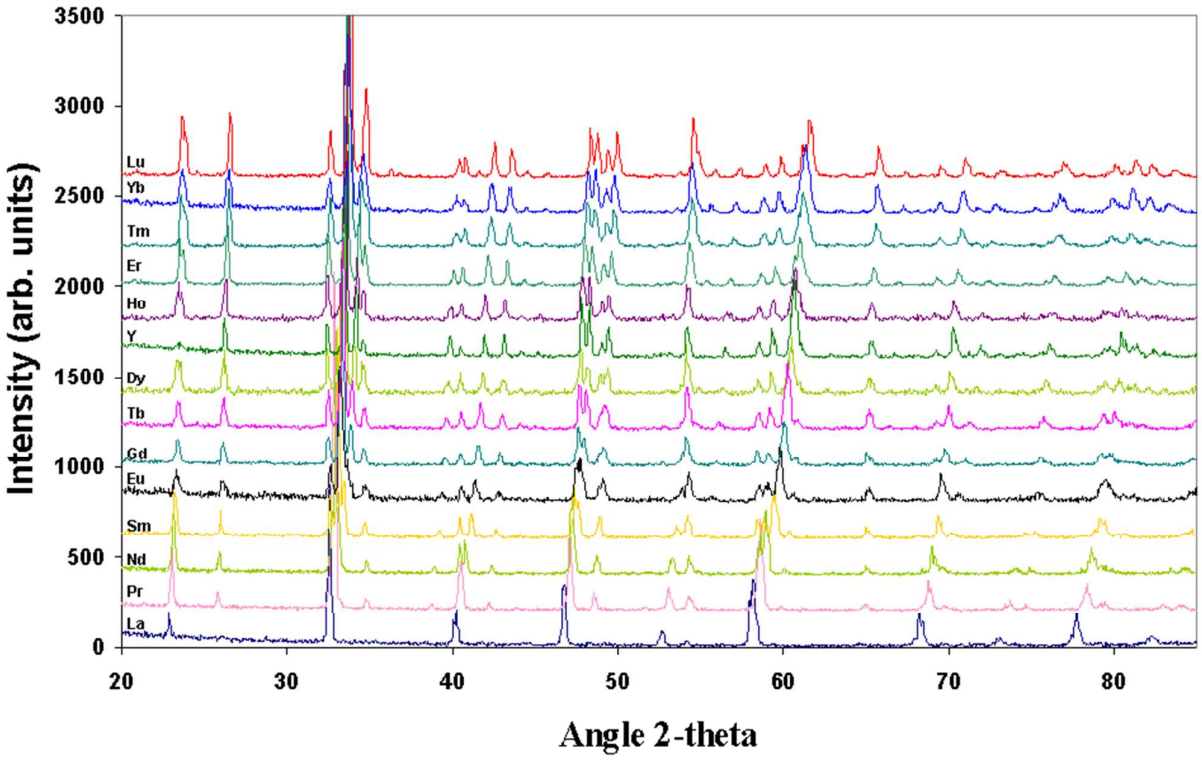

SOM Figure 1: XRD patterns of (RE)CrO_3 powders

Table 1a: Structural parameters for (RE)CrO_3 obtained from refining XRD data

	$LaCrO_3$	$PrCrO_3$	$NdCrO_3$	$SmCrO_3$	$EuCrO_3$	$GdCrO_3$	$TbCrO_3$
***a* (Å)**	5.4790(1)	5.47986(7)	5.48649(3)	5.48848(6)	5.51039(9)	5.52582(7)	5.51909(5)
***b* (Å)**	7.7616(2)	7.7154(1)	7.69419(5)	7.62627(8)	7.6255(1)	7.60635(9)	7.57856(7)
***c* (Å)**	5.5164(1)	5.45034(7)	5.42108(3)	5.35381(6)	5.34191(8)	5.31376(7)	5.29434(5)
RE position 4c							
x	0.0178(2)	0.0354(1)	0.0419(1)	0.0505(1)	0.0541(2)	0.0585(2)	0.0604(2)
z	-0.0035(5)	-0.0074(4)	-0.0087(2)	-0.0103(3)	-0.0119(5)	-0.0131 (4)	-0.0144(3)
U*100 (Å^2)	0.19(2)	0.15(2)	0.27(3)	0.09(2)	0.10(3)	0.28(6)	0.17(3)
Cr position 4b							
U*100 (Å^2)	0.11(2)	0.12(2)	0.17(3)	0.26(3)	0.13(2)	0.13(3)	0.14(2)
O(1) position 4c							
x	0.496(4)	0.483(2)	0.480(1)	0.480 (1)	0.463(2)	0.468(2)	0.465(2)
z	0.064(4)	0.081 (2)	0.089(1)	0.088 (1)	0.095(2)	0.098 (2)	0.100(2)
Occ	1.00(1)	1.00(1)	1.00(2)	1.00(1)	1.00(2)	1.00(2)	1.00(1)
U*100 (Å^2)	0.24(5)	0.11(3)	0.07(2)	0.10(2)	0.24(3)	0.14(3)	0.17(2)
O(2) position 8d							
x	0.280(2)	0.290(2)	0.285(1)	0.285(2)	0.282(2)	0.292 (2)	0.296 (2)
y	0.033(1)	0.033(1)	0.0403(7)	0.0434(9)	0.048(1)	0.048(1)	0.0500(9)
z	-0.271(3)	-0.287(2)	-0.287(1)	-0.290(1)	-0.289(2)	-0.294(2)	-0.298(1)
Occ	1.01(1)	1.00(1)	1.00(1)	1.00(2)	1.00(1)	1.00(2)	1.01(2)
U*100 (Å^2)	0.24(5)	0.11(3)	0.07(2)	0.10(2)	0.24(3)	0.14(3)	0.17(2)
χ^2	1.28	0.93	1.14	2.02	1.41	0.92	0.97
R_{wp} / R_{exp} (%/%)	4.70 / 4.15	4.52 / 4.69	4.53 / 4.25	1.77 / 1.24	3.04 / 2.70	2.68 / 2.78	3.19 / 3.24
R_{Bragg}	**4.29**	3.07	3.89	4.02	4.58	4.68	2.27
S.G. *Pnma*: 4*c* (*x* ¼ *z*), 4*b* (0 0 ½), 8*d* (*xyz*)							

Table 1b: Structural parameters for (RE)CrO_3 from refining XRD data

	$DyCrO_3$	$YCrO_3$	$HoCrO_3$	$ErCrO_3$	$TmCrO_3$	$YbCrO_3$	$LuCrO_3$
***a* (Å)**	5.50805(5)	5.52267(6)	5.50728(5)	5.50289(4)	5.50850(6)	5.48912(5)	5.50150(7)
***b* (Å)**	7.53767(7)	7.53555(8)	7.52026(6)	7.50370(6)	7.50506(8)	7.47059(7)	7.4811(1)
c (Å)	5.25436(5)	5.24376(5)	5.23164(4)	5.21377(4)	5.21114(6)	5.18258(5)	5.17911(7)
RE position 4c							
X	0.0635(1)	0.0666(1)	0.06509(9)	0.06698(7)	0.06766(8)	0.06912(9)	0.0704(1)
Z	-0.0159(2)	-0.0170(2)	-0.0172(1)	-0.01792(10)	-0.0182(1)	-0.0184(1)	-0.0187(2)
U*100 ($Å^2$)	0.11(2)	0.30(4)	0.14(4)	0.04(1)	0.21(1)	0.14(4)	0.08(2)
Cr position 4b							
U*100 ($Å^2$)	0.18(2)	0.29(3)	0.06(2)	0.05(1)	0.18(3)	0.10(4)	0.07(2)
O(1) position 4c							
X	0.467(1)	0.4652 (8)	0.4686(9)	0.46470(77)	0.453 (1)	0.464(1)	0.466(1)
Z	0.101 (1)	0.1044(8)	0.0990(9)	0.10810(77)	0.1136(9)	0.108(1)	0.110(1)
Occ	1.00(1)	1.01(2)	1.01(2)	1.00(1)	1.00(1)	1.01(2)	1.00(2)
U*100 ($Å^2$)	0.31(3)	0.18(3)	0.10(2)	0.13(3)	0.14(5)	0.08(3)	0.11(3)
O(2) position 8d							
X	0.297(1)	0.3023(6)	0.2991(8)	0.30223(65)	0.3019(8)	0.3072(8)	0.303(1)
Y	0.0520 (6)	0.0538(4)	0.0492 (5)	0.05195(41)	0.0562(5)	0.0538(5)	0.0539(7)
Z	-0.3016(9)	-0.3073(6)	-0.3030(8)	-0.30602(63)	-0.3092(7)	-0.3115(8)	-0.307(1)
Occ	1.00(1)	1.01(1)	1.01(2)	1.00(1)	1.00(1)	1.00(1)	1.00(1)
U*100 ($Å^2$)	0.31(3)	0.18(3)	0.10(2)	0.13(3)	0.14(5)	0.08(3)	0.11(3)
χ^2	2.03	1.07	5.05	3.88	1.37	6.32	3.06
R_{wp} / R_{exp} (%/%)	1.62 / 1.13	5.20 / 5.03	4.06 / 1.81	3.43 / 1.74	5.19 / 4.25	4.59 / 1.82	8.15 / 4.66
R_{Bragg} (%)	5.31	2.46	3.20	2.33	1.68	4.40	5.71
S.G. *Pnma*: 4*c* (*x* ¼ *z*), 4*b* (0 0 ½), 8*d* (*xyz*)							

Table 2a: Selected structural information for (RE)CrO_3 obtained from XRD data. Angles are given in degrees and distances in [Å]

	$LaCrO_3$	**$PrCrO_3$**	**$NdCrO_3$**	**$SmCrO_3$**	**$EuCrO_3$**	**$GdCrO_3$**	**$TbCrO_3$**
tolerance factor	0.92338	0.91006	0.90431	0.89315	0.88883	0.88415	0.87984
[a] Tilt angle $\boldsymbol{\theta}$	9.4	11.5	12.2	12.9	13.4	14.4	15.2
[b] Tilt angle $\boldsymbol{\varphi}$	9.4	11.5	12.2	12.9	13.4	14.4	15.2
[c] Tilt angle $\boldsymbol{\mu}$	10.3	13.2	14.4	14.2	16.0	16.1	16.5
Cr-O(1) × 2	1.972(2)	1.981(2)	1.986(2)	1.967(2)	1.968(1)	1.980(3)	1.976(2)
Cr-O(2) × 2	1.94(2)	1.96(1)	1.967(6)	1.955(8)	1.970(3)	1.974(9)	1.970(8)
Cr-O(2)' × 2	2.00(2)	1.98(1)	1.977(6)	1.978(8)	1.985(4)	1.984(9)	1.992(8)
Average *B*'-O	1.971(6)	1.975(4)	1.977(2)	1.966(3)	1.974(1)	1.979(3)	1.980(3)

For S.G. *Pnma* only a *B*-site exists with co-ordination: *B*'-O(1) × 2, *B*'-O(2) × 2 and *B*'-O(2)' × 2

For S.G. *Pnma* the tilting scheme in Glazer's notation ($a^-a^-c^+$) implies that $\boldsymbol{\theta} \approx \boldsymbol{\varphi}$

[a] With [101] for *Pnma*

[b] With [10-1] for *Pnma*

[c] With [010] for *Pnma*

Table 2b: Selected structural information for (RE)CrO_3 obtained from XRD data. Angles are given in degrees and distances in [Å]

	$DyCrO_3$	$YCrO_3$	$HoCrO_3$	$ErCrO_3$	$TmCrO_3$	$YbCrO_3$	$LuCrO_3$
tolerance factor	0.87552	0.87264	0.87156	0.86796	0.86436	0.86076	0.85716
[a] Tilt angle $\boldsymbol{\theta}$	15.9	17.00	15.8	16.6	17.4	17.7	17.0
[b] Tilt angle $\boldsymbol{\varphi}$	15.9	17.00	15.8	16.6	17.4	17.7	17.0
[c] Tilt angle $\boldsymbol{\mu}$	16.6	17.1	16.2	17.6	19.0	17.6	17.8
Cr-O(1) × 2	1.966(2)	1.971(1)	1.958(1)	1.968(1)	1.984(2)	1.960(2)	1.965(2)
Cr-O(2) × 2	1.979(5)	1.988(4)	1.968(4)	1.970(3)	1.983(4)	1.972(5)	1.968(6)
Cr-O(2)' × 2	1.979(5)	1.993(3)	1.978(4)	1.985(4)	1.991(4)	1.990(5)	1.984(6)
Average *B*'-O	1.975(2)	1.984(1)	1.968(2)	1.974(1)	1.986(1)	1.974(2)	1.972(2)

For S.G. *Pnma* only a *B*-site exists with co-ordination: *B*'-O(1) × 2, *B*'-O(2) × 2 and *B*'-O(2)' × 2

For S.G. *Pnma* the tilting scheme in Glazer's notation ($a^-a^-c^+$) implies that $\boldsymbol{\theta} \approx \boldsymbol{\varphi}$

[a] With [101] for *Pnma*

[b] With [10-1] for *Pnma*

[c] With [010] for *Pnma*

Part II. Scanning electron microscopy

SOM Figure 2 shows the SEM micrographs for the powders of the $(RE)CrO_3$ series, where clearly different agglomeration behavior of the crystallite particles is demonstrated. The RE cation appears to play an important role in determining the agglomeration behavior.

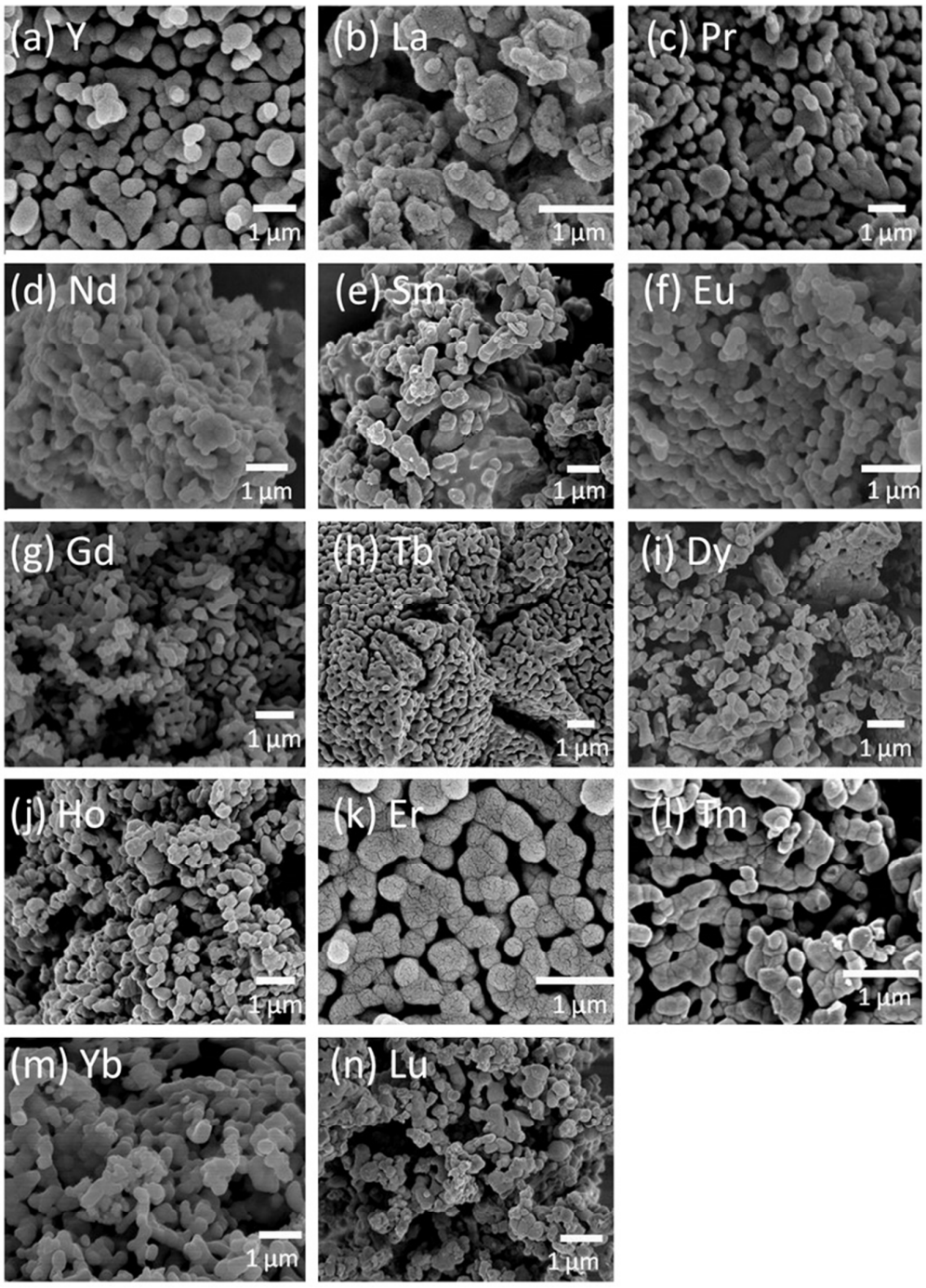

SOM Figure 2: SEM micrographs of $(RE)CrO_3$ powder

Part III. Raman spectroscopy

The positions of several selected Raman modes and how they develop across the $(RE)CrO_3$ series are summarized in Table 3. SOM Figure 3 shows plots of Raman wave number vs RE ionic radius IOR for several selected modes. It can be seen that certain Raman modes show stronger dependence on IOR than others. The positions of the $A_g(3)$ and $A_g(5)$ Raman modes with the strongest dependence on IOR are plotted in SOM Figure 4 vs octahedral perovskite tilting angle to highlight an approximately linear dependence.

Table 3: Wave numbers of selected Raman modes for $(RE)CrO_3$

$(RE)CrO_3$	**Raman mode wave numbers in [cm^{-1}]**							
	$A_g(2)$	$A_g(3)$	$A_g(4)$	$A_g(5)$	$A_g(6)$	$B_{1g}(2)$	$B_{2g}(1)$	$B_{3g}(3)$
$LaCrO_3$	120	154	254	278	442	353	135	594
$PrCrO_3$	133	196	281	324	454	371	152	583
$NdCrO_3$	130	192	278	320	451	367	144	579
$SmCrO_3$	140	235	312	368	470	387	155	572
$EuCrO_3$	135	235	306	372	460		149	557
$GdCrO_3$	143	257	328	394	482		162	574
$TbCrO_3$	139	259	329	395	478		154	561
$DyCrO_3$	145	269	344	415	492	405	164	572
$YCrO_3$	(189)	284	345	429	495	412	(221)	569
$HoCrO_3$	144	278	344	423	500	409	163	571
$ErCrO_3$	149	282	353	442	(520)	(395)	168	575
$TmCrO_3$	144	282	353	442	506	414	163	571
$YbCrO_3$	144	282	358	451	511	418	168	580
$LuCrO_3$	138	291	356	454	515	417	162	

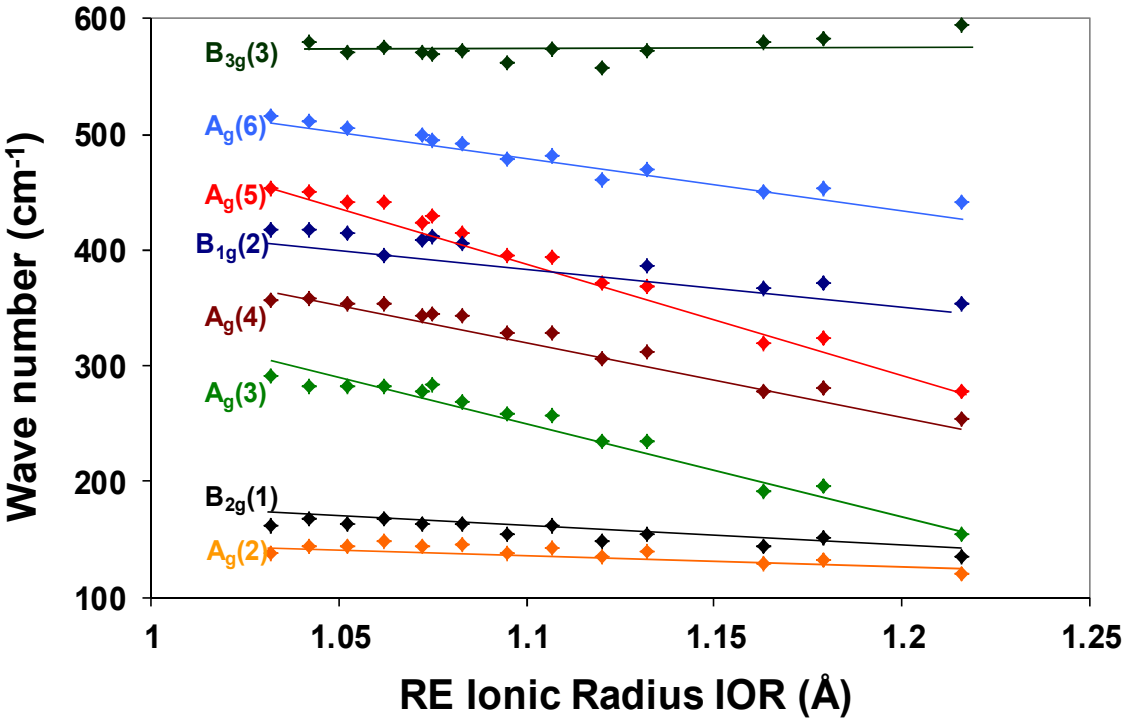

SOM Figure 3: Wave numbers of selected Raman modes in (RE)CrO_3 vs IOR.

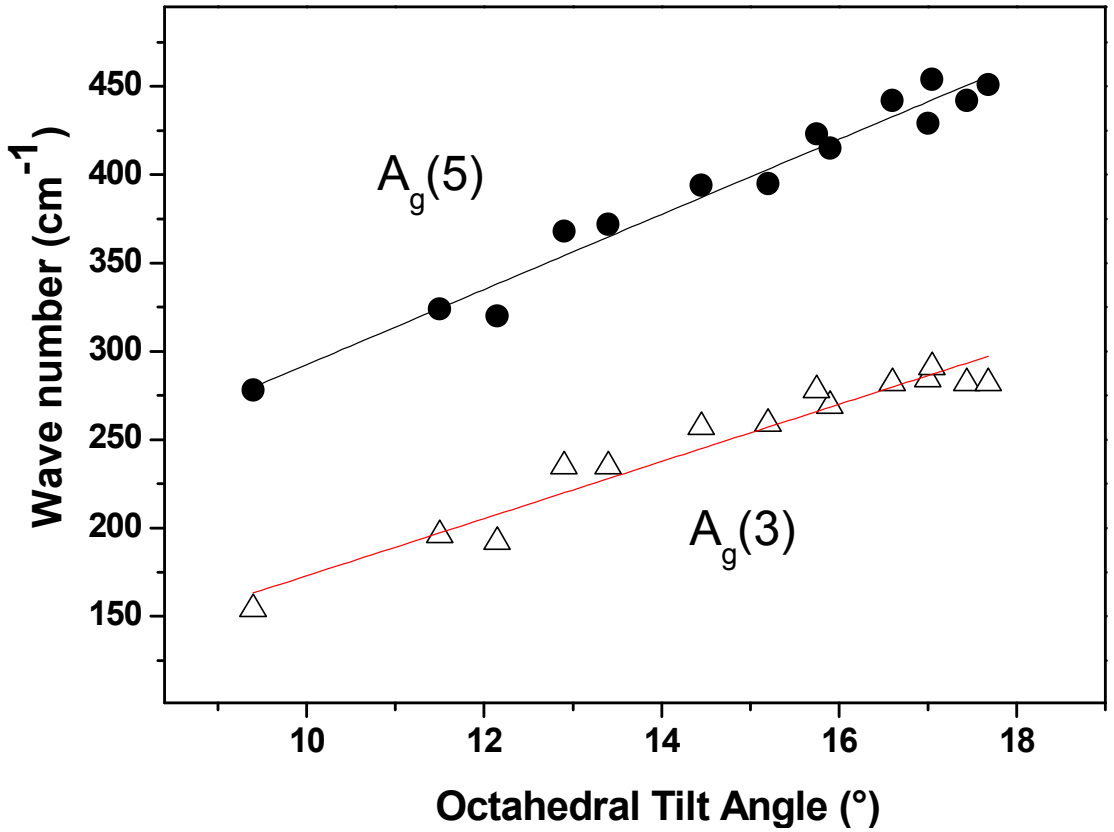

SOM Figure 4: Wave numbers vs octahedral tilt angle θ. Solid lines are guide to the eyes.

Part IV. Magnetic structure

Table 4 shows the magnetic parameters extracted from magnetization vs temperature curves (Neel temperatures T_{N1}, T_{N2}) and from Curie-Weiss fits (Curie and Weiss constants C, Θ, and effective magnetization μ_{eff}). The Neel temperature T_{N1} marks the onset of antiferromagnetic Cr^{3+}-Cr^{3+} ordering, T_{N2} marks the onset of antiferromagnetic ordering of the $(RE)^{3+}$ spins.

Table 4: Magnetic parameters for $(RE)CrO_3$ obtained from magnetization measurements

	T_{N1} Cr^{3+} (K)		T_{N2} RE^{3+} (K)		C (μ_B)	Θ (K)	Total μ_{eff} (μ_B)	
$(RE)CrO_3$	Experim.	Literature	Experim.	Literature[1,2]			Experim.	Theoretical
$LaCrO_3$	288	282	-	-	-	-	-	3.87
$PrCrO_3$	239	239	2	2	3.3	-160	5.15	5.21
$NdCrO_3$	226	224	11	10	3.8	-189	5.54	5.29
$SmCrO_3$	191	193	-	-	3.4	-314	5.21	5.46
$EuCrO_3$	185	181	-	-	3.4	-198	5.23	5.15
$GdCrO_3$	171	170	3	4	7.3	-29	7.65	8.83
$TbCrO_3$	159	158	4.5	4	12.9	-26	10.17	10.46
$DyCrO_3$	149	146	2	2	15.7	-24	11.21	11.33
$YCrO_3$	141	140	-	-	2.51	-408	4.48	3.87
$HoCrO_3$	142	141	-	12	15.7	-21	11.22	11.28
$ErCrO_3$	136	133	14	17	12.8	-24	10.12	10.33
$TmCrO_3$	125	124	3	4	8.6	-32	8.30	8.49
$YbCrO_3$	120	118	4	3	4.4	-99	5.92	5.97
$LuCrO_3$	109	112	-	-	2.4	-174	4.42	3.87

1.) Goodenough J.B., Longo J.M.: *Landolt-Börnstein New Series III*, ed. Hellwege K.-H., Hellwege A.M. (Springer, Berlin, **1970**) Vol.4, Part A, p.228. **2.)** Sardar K., Lees M. R., Kashtiban R. J., Sloan J., Walton R. I., Chem. Mater. **2011**, *23*, 48

The effective magnetic moments μ_{eff}, originating from the Cr^{3+} cations were calculated from the Curie constants C according to $\mu_{eff}^2 = 8C$. The theoretical value for μ_{eff} was regarded a combination of Cr^{3+} and $(RE)^{3+}$, where $\mu_{eff}(Cr^{3+}) = 3.87\ \mu_B$, obtained from the equation $\mu_{eff} = 2[S(S+1)]^{1/2}$ with the multiplicity S = 3/2. For $(RE)^{3+}$ $\mu_{eff} = g_L[J(J+1)]^{½}$ where g_L is the Landé g-factor ($g_L = (3/2)+[(S(S+1)-L(L-1))/2J(J+1)]$), J is the total angular momentum and L corresponds to the maximum orbital angular momentum. All μ_{eff} values are displayed in SOM Figure 5, together with theoretical values in agreement with Landolt-Börnstein tables. For the $LaCrO_3$ sample T_{N1} is high and no sufficient $1/\chi$ vs T data points were available at high T to perform a Curie-Weiss fit.

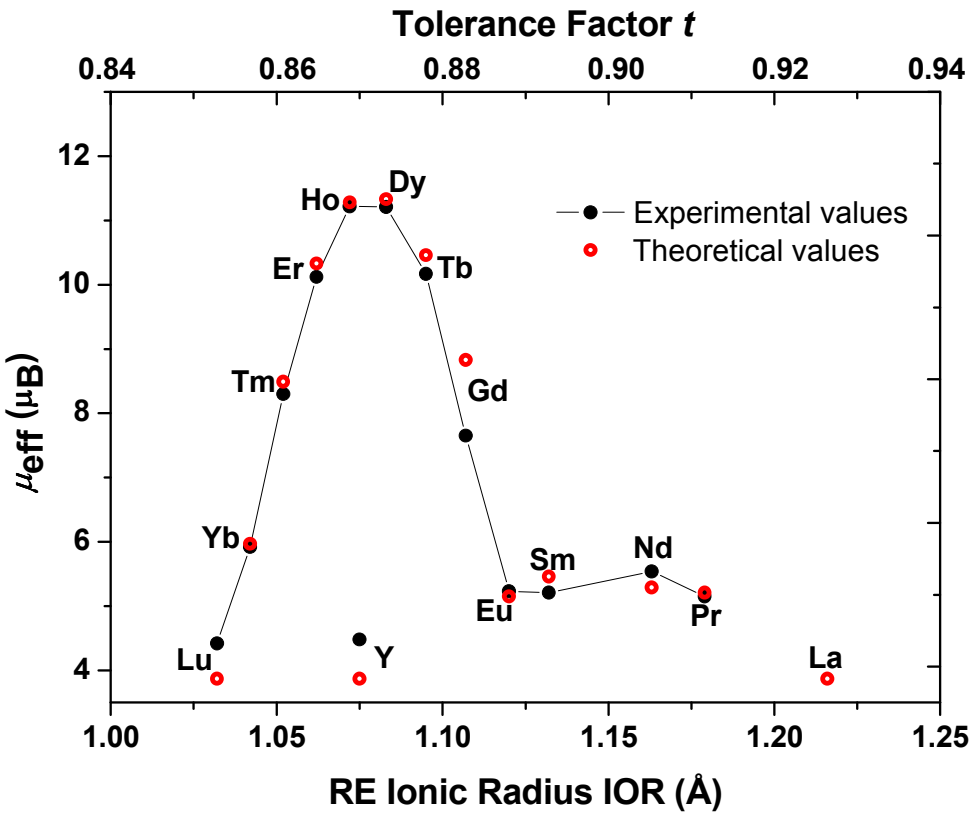

SOM Figure 5 Effective magnetic moment μ_{eff} for the $(RE)CrO_3$ series as determined from the respective Curie-Weiss fits and plotted vs IOR. Theoretical values were calculated from Landolt-Börnstein tables.

Part V. Dielectric spectroscopy

The impedance spectroscopy data obtained for all pellets from the $(RE)CrO_3$ series were analyzed to extract bulk and GB resistivity (ρ_1, ρ_2) and permittivity (ε_1, ε_2). The bulk and GB relaxations were approximated by an equivalent circuit consisting of two ideal RC elements connected in series (see Inset in SOM Figure 6), where the non-ideality was neglected. R1 and C1 describe the intrinsic bulk resistivity ρ_1 and bulk permittivity ε_1 respectively, whereas R2 and C2 describe the extrinsic GB resistivity ρ_2 and GB permittivity ε_2 respectively. The ρ_1, ρ_2, ε_1 and ε_2 values were extracted by the following procedure:

1.) The bulk and GB resistivity values ρ_1 and ρ_2 were obtained from the estimated diameter of the respective semicircle in the $-Z''$ vs Z' plots.

2.) The bulk and GB permittivity values ε_1 and ε_2 were obtained from the peak frequency f_{max} of the bulk or GB dielectric relaxation peaks according to equation (1) shown below. The bulk dielectric relaxation peak was displayed clearly in plots of the imaginary part of the modulus function M'' vs f (SOM Figure 6, upper panel), whereas the GB peak was best displayed in plots of $-Z''$ vs f (SOM Figure 6, lower panel).

In SOM Figure 6 the curves for the Ho-, Gd-, Pr-, and Y-containing samples are shifted up the M'' and $-Z''$ y-axes by increasing amounts for demonstration purposes. The $-Z''$ vs f curves were normalized to render the peak heights comparable to enable equivalent resolution for all samples within the same graph.

The approximate conditions for a bulk or GB relaxation peak maximum to occur are shown in equation 1 for both notations, M'' vs f and $-Z''$ vs f, using the framework of the brick work layer and RC element model for ideal relaxations. The approximate peak ordinates are distinctively different for $M''(f_{max})$ and $-Z''(f_{max})$ (equation 2), which guarantees that in the M'' vs f notation the smallest capacitance (bulk) and in the $-Z''$ vs f notation the largest resistance (GB) are most strongly pronounced.

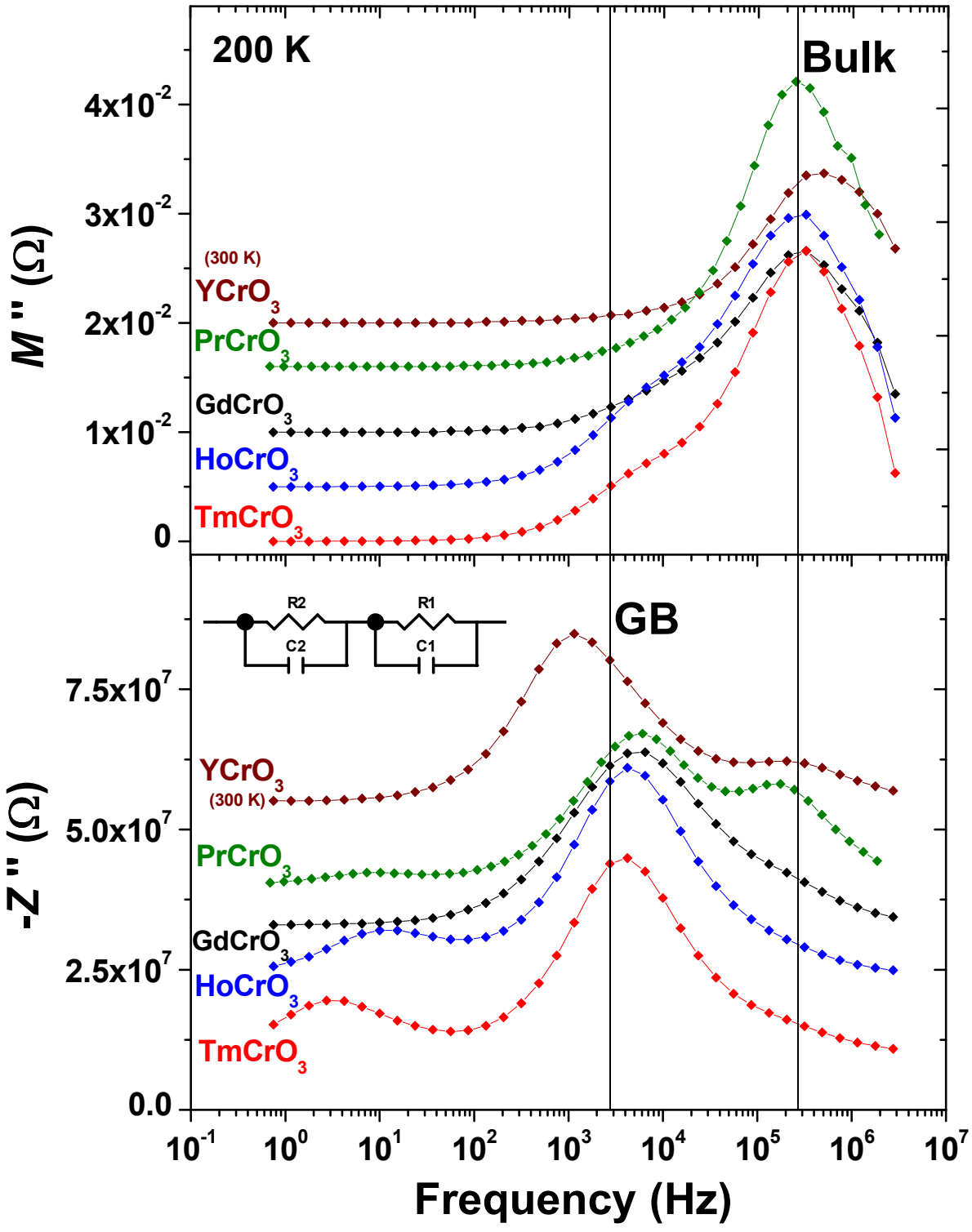

SOM Figure 6 Comparison of modulus and impedance spectroscopy for 5 representative examples from the (RE)CrO_3 series. The bulk dielectric relaxation peaks dominate the M'' vs f curves, whereas the GB peaks are strongly pronounced in the $-Z''$ vs f curves.

This is clearly evident in SOM Figure 6, where the main bulk peaks in M'' vs f clearly dominate over the secondary GB peaks, whereas the main GB peaks in $-Z''$ vs f clearly dominate over the secondary bulk peaks. In fact, some of the secondary peaks cannot be resolved at all in the respective notation.

$$f_{\max}(M'') \approx \frac{1}{2\pi\ \rho_1 \varepsilon_0 \varepsilon_1}\ ;\ f_{\max}(-Z'') \approx \frac{1}{2\pi\ \rho_2 \varepsilon_0 \varepsilon_2}\quad ; \qquad \text{(eq.1)}$$

$$M''(f_{\max}) \approx \frac{1}{2\varepsilon_1}\ ;\ -Z''(f_{\max}) \approx \frac{\rho_2}{2}\quad ; \qquad \text{(eq.2)}$$

The resistivity values obtained were plotted on Arrhenius axes and the activation energies E_A were determined. The bulk and GB activation energies, dielectric permittivity and the resistivity at 200 K are summarized in Table 5. The bulk and GB resistivity vs reciprocal temperature curves are presented in the SOM Figures 7 and 8, whereas the bulk permittivity values vs temperature plots are shown in SOM Figure 9. The bulk permittivity ε_1 vs T curves show considerable scatter in several instances, which is a reflection of the limited accuracy of the manual data analysis method employed.

Table 5: Dielectric parameter for (RE)CrO_3 obtained from impedance spectroscopy

(RE)CrO_3	Activation Energy E_A in [eV]		Dielectric Permittivity [dimensionless]		Resistivity at 200 K in [Ωcm]	
	Bulk	GB	Bulk ε_1	GB ε_2	Bulk ρ_1	GB ρ_2
$LaCrO_3$	0.22	0.29	15.6	2520	$3.92\ 10^6$	$4.45\ 10^5$
$PrCrO_3$	0.21		17.2	407	$4.11\ 10^5$	$8.89\ 10^5$
$NdCrO_3$	0.23	0.3	15.8	258	$5.17\ 10^4$	$1.96\ 10^7$
$SmCrO_3$	0.22	0.26	23.7	90.2		
$EuCrO_3$	0.26	0.29	18.7	283	$1.70\ 10^5$	$6.93\ 10^6$
$GdCrO_3$	0.27	0.31	27.1	177	$1.96\ 10^5$	$1.93\ 10^6$
$TbCrO_3$		0.30	12.5	318	$1.05\ 10^7$	$8.40\ 10^6$
$DyCrO_3$	0.27	0.28	17.3	47.4	$5.40\ 10^5$	$1.15\ 10^7$
$YCrO_3$	0.32	0.33	21.7	1740	$8.00\ 10^7$	$5.04\ 10^8$
$HoCrO_3$	0.26	0.28	12.9	76.8	$4.27\ 10^5$	$5.62\ 10^6$
$ErCrO_3$	0.27	0.29	14.1	181	$4.27\ 10^5$	$2.42\ 10^6$
$TmCrO_3$	0.25	0.29	14.4	102	$3.93\ 10^5$	$4.66\ 10^6$
$YbCrO_3$	0.28		19.6	164	$1.97\ 10^6$	$1.14\ 10^{10}$
$LuCrO_3$	0.28	0.27	20.0	97.4	$1.28\ 10^6$	$3.11\ 10^7$

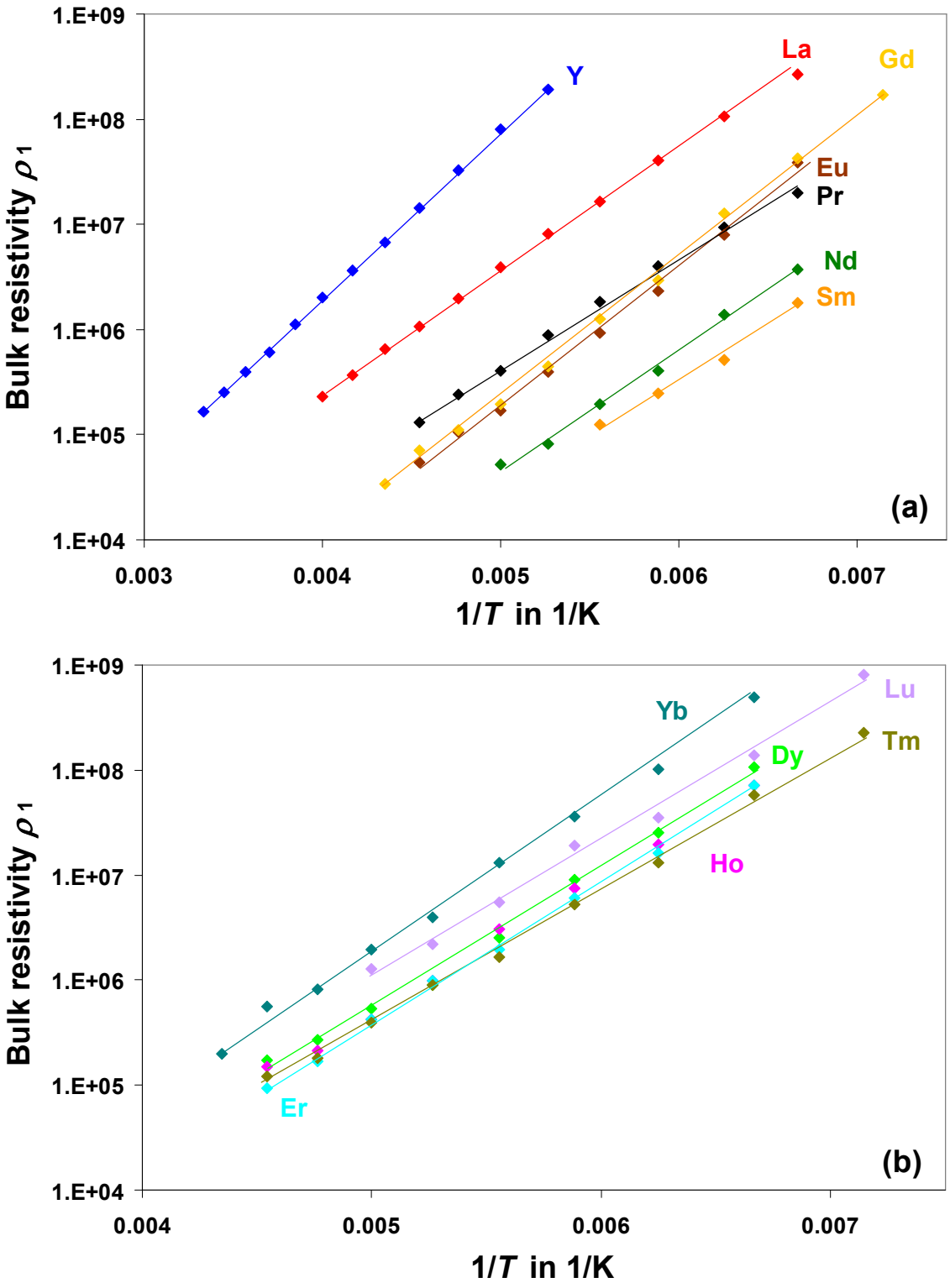

SOM Figure 7a & b: Bulk resistivity ρ_1 plotted vs reciprocal temperature $1/T$. Solid lines are guide to the eyes, indicating good linearity and Arrhenius behavior.

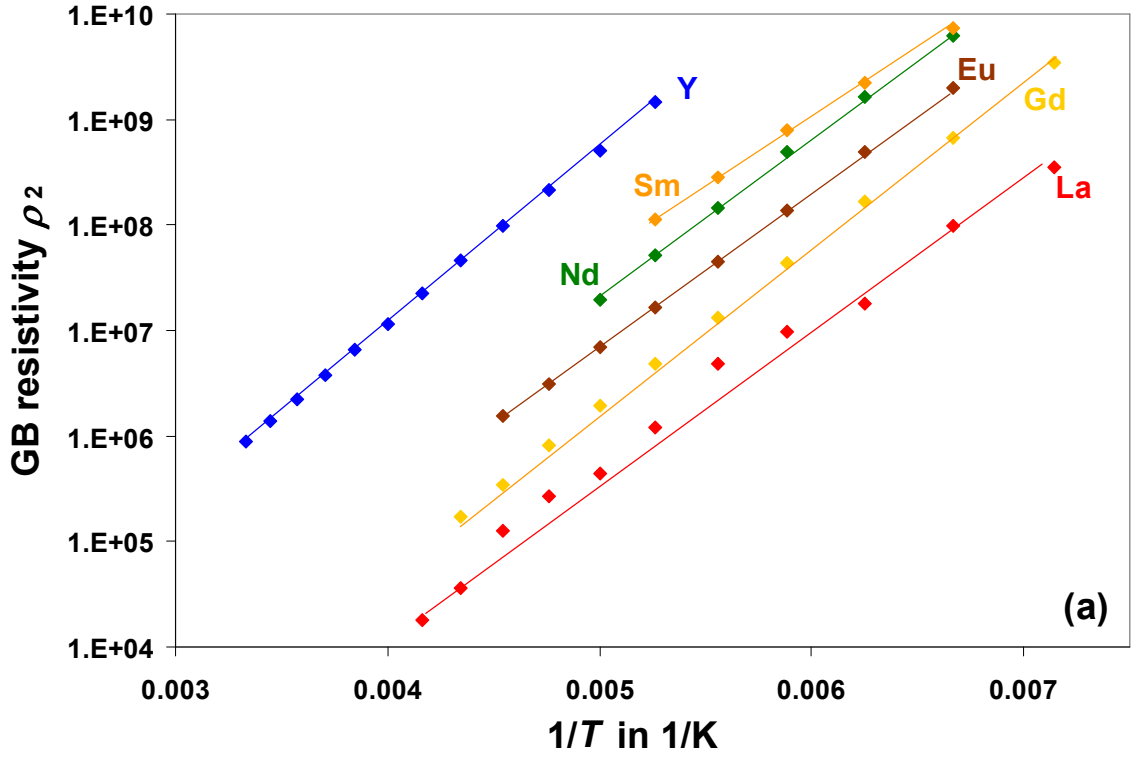

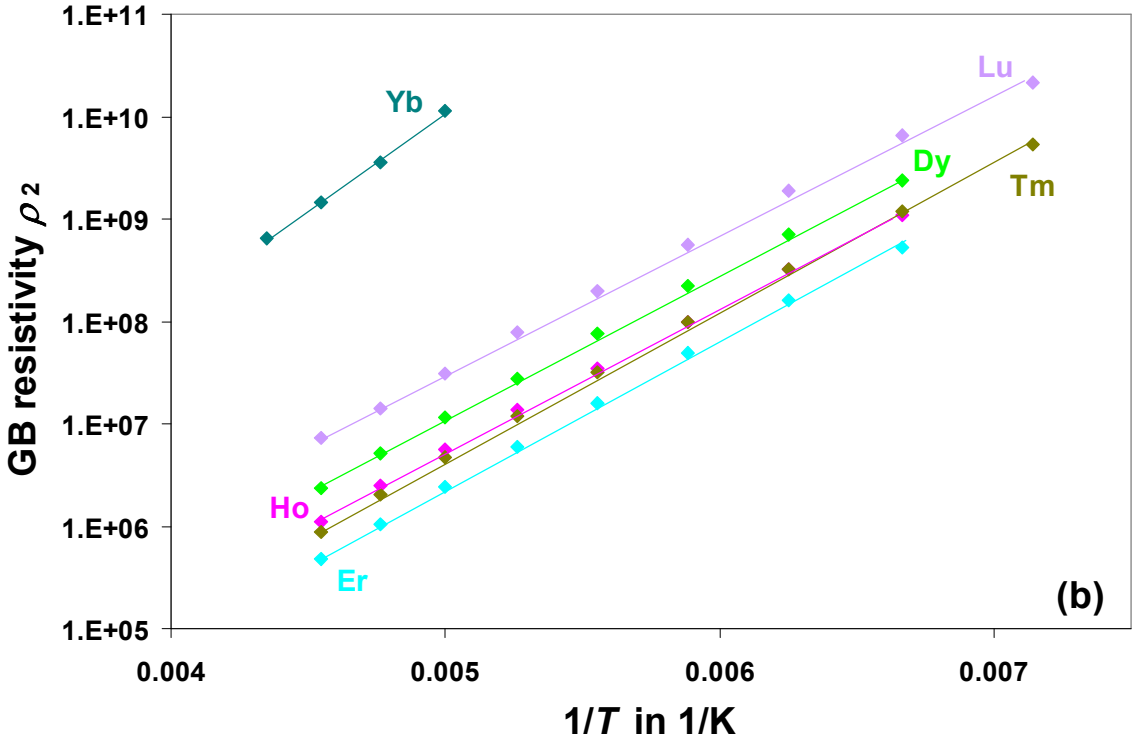

SOM Figure 8a & b: GB resistivity ρ_2 plotted vs reciprocal temperature $1/T$. Solid lines are guide to the eyes, indicating good linearity and Arrhenius behavior.

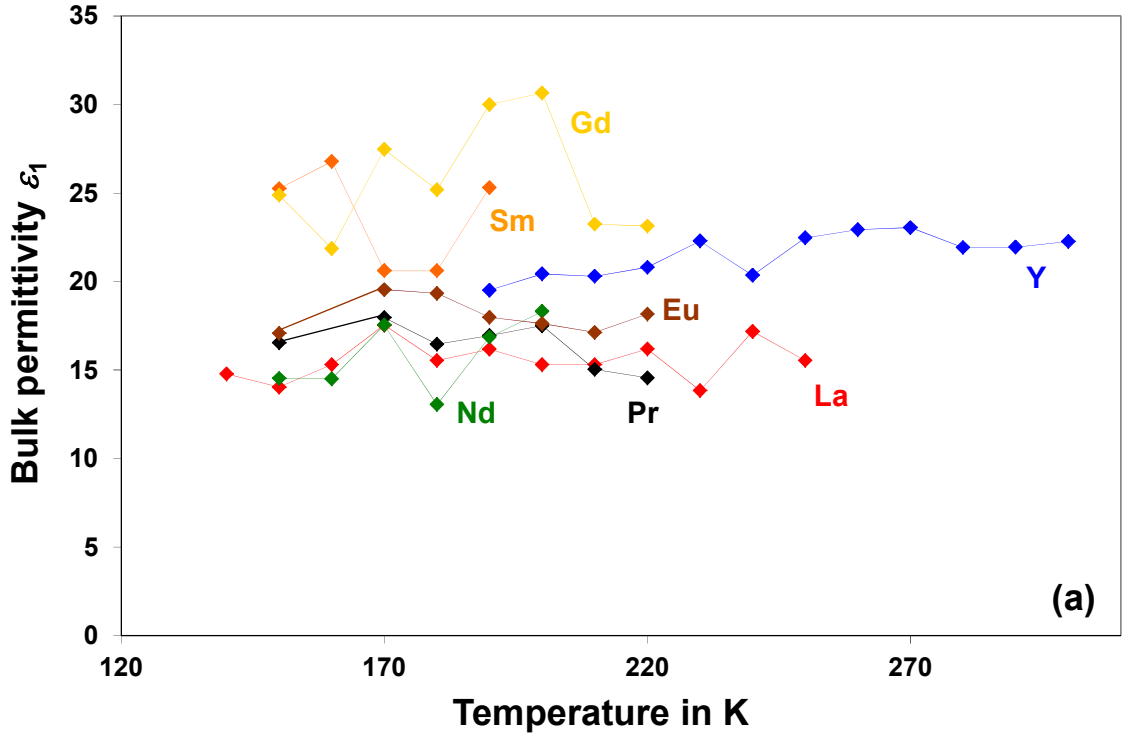

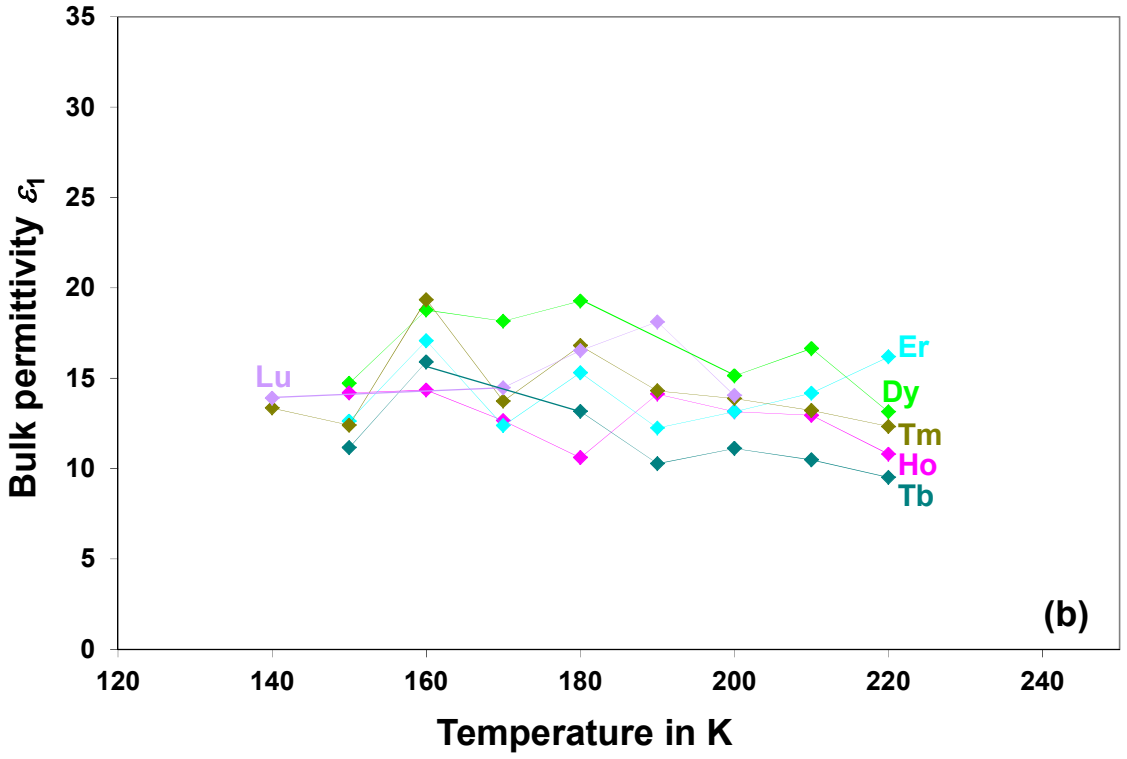

SOM Figure 9a & b: Bulk permittivity ε_1 plotted vs temperature T. In several curves the data scatter is considerable as a reflection of the limited accuracy of the manual data analysis.